

Electromagnetic absorption and Kerr effect in quantum Hall ferromagnetic states of bilayer graphene

R. Côté,¹ Manuel Barrette,¹ and Élie Bouffard¹

¹*Département de physique, Université de Sherbrooke, Sherbrooke, Québec, J1K 2R1, Canada*

(Dated: November 7, 2018)

In a quantizing magnetic field, the chiral two-dimensional electron gas in Landau level $N = 0$ of bilayer graphene goes through a series of phase transitions at integer filling factors $\nu \in [-3, 3]$ when the strength of an electric field applied perpendicularly to the layers is increased. At filling factor $\nu = 3$, the electron gas can be described by a simple two-level system where layer and spin degrees of freedom are frozen. The gas then behaves as an orbital quantum Hall ferromagnet. A Coulomb-induced Dzyaloshinskii-Moriya term in the orbital pseudospin Hamiltonian is responsible for a series of transitions first to a Wigner crystal state and then to a spiral state as the electric field is increased. Both states have a non trivial orbital pseudospin texture. In this work, we study how the phase diagram at $\nu = 3$ is modified by an electric field applied in the plane of the layers and then derive several experimental signatures of the uniform and nonuniform states in the phase diagram. In addition to the transport gap, we study the electromagnetic absorption and the Kerr rotation due to the excitations of the orbital pseudospin-wave modes in the broken-symmetry states.

PACS numbers: 73.21.-b, 73.22.Gk, 78.67.Wj

I. INTRODUCTION

In a Bernal-stacked graphene bilayer (BLG), electrons behave as a chiral two-dimensional Fermi gas.¹ When quantized by a strong perpendicular magnetic field and when Coulomb interaction is considered, a rich set of phase transitions occurs in Landau level $N = 0$ ²⁻⁴ as well as in higher Landau levels $|N| > 0$.⁵ The diversity of phases is greater in level $N = 0$ which has an extra orbital degree of freedom $n = 0, 1$ in addition to the valley $\xi = \pm 1$ (for valleys K_{\pm}) and spin $\sigma = \pm 1$ quantum numbers shared by all the other Landau levels. At a fixed magnetic field, and in a transverse electric field E_{\perp} , a different sequence of phase transitions is obtained at each filling factor $\nu \in [-3, 3]$ in $N = 0$ when a potential difference $\Delta_B = E_{\perp}d$ (or bias) between the two layers with separation d is increased.

The various phases driven by the bias Δ_B can be described as quantum Hall ferromagnets (QHF's). In the pseudospin language, the two spin, valley, and orbital indices are mapped into a $1/2$ spin, valley pseudospin and orbital pseudospin respectively. In the simplest tight-binding model where only in-plane and inter-plane hoppings γ_0 and γ_1 are considered (see below for a more precise definition of these terms) and in the absence of Coulomb interaction, Zeeman and bias couplings, all eight states in $N = 0$ are degenerate. However, additional couplings such as the γ_4 hopping term breaks the orbital degeneracy while a Zeeman or a bias term break the spin and the valley degeneracy respectively. The degeneracy can also be spontaneously broken by the Coulomb interaction leading to different types of quantum Hall ferromagnetic states. At the Hartree-Fock level, it has been shown that Coulomb interaction completely lifts the degeneracy of the $N = 0$ octet leading to the formation of seven new plateaus in the Hall conductivity.^{3,6} These plateaus have been detected experimentally.⁷

Most of the research done so far on the QHF's in $N = 0$ has considered uniform states. But, at special filling factors $\nu = 1, 3$, a sequence of phase transitions involving uniform and nonuniform states is also possible.^{3,8,9} The nonuniform states occur in a region of bias where the system can be described as an orbital QHF i.e. where the electrons collectively condense into a linear combination of the $n = 0$ and $n = 1$ orbitals. The sequence of transitions for $\nu = 3$ is represented schematically in Fig. 1 below. It involves spiral and crystal states where the orbital pseudospin is modulated in pseudospin space as well as uniform states with and without orbital coherence. The rotation of the pseudospin is induced by an effective Dzyaloshinskii-Moriya (DM) interaction due to the Coulomb exchange term in the Hamiltonian. There is no spin-orbital coupling in the 2DEG. The sequence of transitions in Fig. 1 is similar to that uncovered in helical magnets such as MnSi and Fe_{1-x}Co_xSi¹⁰. In these systems, however, the transitions are induced by changing the magnetic field.

In Refs. 8 and 9, some of us have studied several aspects of the phase diagram in Fig. 1: the order parameters, the density of states, the band structure, the collective excitations. In the present work, we study in more detail possible transport and optical experimental signatures of the different phases in this diagram that have, so far, not been detected experimentally. Optical spectroscopy has been used extensively to study graphene and multilayer graphene structures (see Ref. 11 for an overview of the subject). This includes absorption from Landau level transitions and Faraday and Kerr effects (optical polarization rotation of the transmitted and reflected wave respectively). The Faraday rotation, in particular, was shown to be very large in graphene.¹² Optical methods can also be used to study broken-symmetry states.¹³ Indeed, the signatures of several gapped states on the optical conductivity of bilayer graphene have been

studied in some detail in Ref. 14 but this did not include the nonuniform states that we considered in this article.

Optical transitions between non-interacting states in BLG¹¹ must satisfy the selection rule $|N\rangle \rightarrow |N| \pm 1$ and are naturally classified as right and left circularly polarized transitions because of the change in orbital momentum between the two levels involved in the transition. The same division occurs in the simple case of $\nu = 3$ in $N = 0$ where the system can effectively be mapped into a two-level system with orbital degrees of freedom $n = 0, 1$ and where spin and valley indices are polarized. (The phase diagram is slightly more complex for $\nu = 1$ and includes states with spin coherence.) In the left of the phase diagram in Fig. 1 (i.e. for bias $\Delta_B < \Delta_M$ where Δ_M defines the middle of the spiral state), electrons occupy mostly the $n = 0$ states and optical absorption in all phases occurs for transition from $n = 0$ to $n = 1$. Just the opposite is true in the right of the phase diagram (for bias $\Delta_B > \Delta_M$) where electrons occupy mostly the $n = 1$ states. As we will show, a spontaneous uniform orbital QHF does not lead to absorption at finite frequency since its pseudospin-wave mode is gapless. The other phases, however, have modes that can be excited with right or left circularly polarized light. It should thus be possible to distinguish the phases by the optical absorption due to their collective modes. In Fig. 1, pairs of states (or "conjugate states") on each side of Δ_M share the same dispersion of their collective modes as well as other physical properties such as the transport gap. They absorb electromagnetic radiation at the same frequency although with different intensities and from opposite circular polarizations of an incident electromagnetic wave. The Kerr rotation also show noticeably different behaviors for conjugate biases: the polarization rotates in opposite directions and the amplitude of the rotation is much larger for bias $\Delta_B > \Delta_M$. The symmetry of the phase diagram is such there can be no Kerr effect at $\Delta_B = \Delta_M$.

We extend our previous study of the phase diagram^{3,8,9} to the case where there is an electric field applied in a direction parallel to the layers. It was shown before that such a field would gap the orbital pseudospin Goldstone mode of the uniform phase with orbital coherence¹⁵. We show in this work how the phase diagram is modified by such a field, how the collective modes dispersion are changed in the various phases and finally how this field affects the optical absorption.

This paper is organized as follow. We describe in Sec. II the 2DEG at filling factor $\nu = 3$ as an effective two-level system with frozen valley and spin degrees of freedom. We derive in Sec. III the phase diagram at $\nu = 3$ when one of the two level is filled. In Sec. IV, we consider the effect of a parallel electric field on the phase diagram. In Secs. V and VI, we derive the optical absorption and Kerr effect due to the collective excitations. We conclude in Sec. VII. To avoid repetitions, we refer the reader to previous works in Refs. 3,8,9, where the Hartree-Fock method for deriving the phase diagram and the calculation of the collective modes in the generalized

random-phase approximation (GRPA) are described in detail.

II. THE 2DEG AT $\nu = 3$ AS A TWO-LEVEL SYSTEM

The system considered in this work is a Bernal-stacked graphene bilayer (BLG) in a transverse magnetic $\mathbf{B} = B\hat{\mathbf{z}}$ and electric $\mathbf{E} = E\hat{\mathbf{z}}$ fields. The electric field induces a potential difference (or *bias*) $\Delta_B = Ed$ between the two layers separated by a distance $d = 3.34$ Å. The honeycomb lattice in each of these layers is described as a triangular Bravais lattice with a basis of two carbon atoms A_n and B_n , where $n = 1, 2$ is the layer index and the lattice constant is $a_0 = 2.46$ Å. The unit cell has four lattice sites denoted by $\{A_1, B_1, A_2, B_2\}$. The reciprocal lattice has an hexagonal Brillouin zone with two non-equivalent valleys $K_\xi = \left(\frac{2\pi}{a_0}\right)(\xi\frac{2}{3}, 0)$, where $\xi = \pm 1$.¹ In the Bernal stacking arrangement, the upper A sublattice is directly on top of the lower B sublattice while the upper B sublattice is above the center of a hexagonal plaquette of the lower layer.

For a neutral bilayer, the chemical potential is at the energy $E = 0$ and the low-energy excitations ($E \ll \gamma_1$) can be studied using an effective two-component model¹⁶ with an Hamiltonian, in the absence of the quantizing magnetic field, given by

$$H_{\xi,\sigma}^0(\mathbf{p}) = \begin{pmatrix} \xi\frac{\Delta_B}{2} + \eta_{-\xi}p_-p_+ & \frac{1}{2m^*}p_-^2 \\ -\frac{1}{2}\sigma\Delta_Z & -\xi\frac{\Delta_B}{2} + \eta_{\xi}p_+p_- \\ \frac{1}{2m^*}p_+^2 & -\frac{1}{2}\sigma\Delta_Z \end{pmatrix}. \quad (1)$$

This Hamiltonian is here written in the basis (A_2, B_1) for valley K_- and (B_1, A_2) for valley K_+ and $p_\pm = p_x \pm ip_y$. The parameter

$$\eta_\xi = \frac{1}{2m^*} \left(\xi\frac{\Delta_B}{\gamma_1} + 2\frac{\gamma_4}{\gamma_0} + \frac{\delta_0}{\gamma_1} \right), \quad (2)$$

with the effective mass $m^* = 2\hbar^2\gamma_1/3\gamma_0^2a_0^2$, where $\gamma_0 = 2.61$ eV¹⁷ is the in-plane nearest-neighbor hopping, $\gamma_1 = -0.361$ eV is the interlayer hopping between carbon atoms that are immediately above one another (i.e. $A_1 - B_2$) and $\gamma_4 = -0.138$ eV is the interlayer next nearest-neighbor hopping term between carbons atoms in the same sublattice (i.e. $A_1 - A_2$ and $B_1 - B_2$). The parameter $\delta_0 = 0.015$ eV represents the difference in the crystal field between sites A_1, B_2 and A_2, B_1 . We ignore the warping term γ_3 , a valid approximation at the magnetic fields considered in this article.^{16,18} The Zeeman coupling $\Delta_Z = g\mu_B B$, where $g = 2$ and $\sigma = \pm 1$ is the spin index.

A quantizing perpendicular magnetic field is taken into account by making the Peierls substitution $\mathbf{p} \rightarrow \mathbf{P} = \mathbf{p} + e\mathbf{A}/c$ (with $e > 0$), where $\nabla \times \mathbf{A} = B\hat{\mathbf{z}}$. Defining

the ladder operators $a = (P_x - iP_y)\ell/\sqrt{2}\hbar$ and $a^\dagger = (P_x + iP_y)\ell/\sqrt{2}\hbar$ and the magnetic length $\ell = \sqrt{\hbar c/eB}$, we get

$$H_{\xi,\sigma}^0 = \begin{pmatrix} \xi \frac{\Delta_B}{2} + \zeta_- aa^\dagger & \zeta' a^2 \\ -\frac{1}{2}\sigma\Delta_Z & \\ \zeta' (a^\dagger)^2 & -\xi \frac{\Delta_B}{2} + \zeta_+ a^\dagger a \\ -\frac{1}{2}\sigma\Delta_Z & \end{pmatrix}, \quad (3)$$

where

$$\zeta = \beta \left(2 \frac{\gamma_1 \gamma_4}{\gamma_0} + \delta_0 \right), \quad (4)$$

$$\zeta_\pm = \zeta \pm \xi \beta \Delta_B, \quad (5)$$

$$\zeta' = \beta \gamma_1 \left(1 + 2 \frac{\delta_0 \gamma_4}{\gamma_0 \gamma_1} + \left(\frac{\gamma_4}{\gamma_0} \right)^2 \right), \quad (6)$$

and

$$\beta = \frac{\hbar \omega_c^*}{\gamma_1} = 7.24 \times 10^{-3} B [\text{T}], \quad (7)$$

where the effective cyclotron frequency $\omega_c^* = eB/m^*c$ with

$$\hbar \omega_c^* = 2.61 B [\text{T}] \text{ meV}. \quad (8)$$

In Eq. (3), the ladder operators are defined by $a^\dagger \varphi_n(x) = i\sqrt{n+1} \varphi_{n+1}(x)$ and $a \varphi_n(x) = -i\sqrt{n} \varphi_{n-1}(x)$, where $\varphi_n(x)$ (with $n = 0, 1, 2, \dots$) are the eigenfunctions of the one-dimensional harmonic oscillator.

The two-component model describes well¹⁸ the eigenenergies and eigenstates of the Landau level $N = 0$ which has eight sub-levels indexed by the quantum numbers ξ and σ and an extra "orbital" index $n = 0, 1$. The eigenenergies are

$$E_{\xi,\sigma,n=0} = -\xi \frac{\Delta_B}{2} - \sigma \frac{\Delta_Z}{2}, \quad (9)$$

$$E_{\xi,\sigma,n=1} = -\xi \frac{\Delta_B}{2} - \sigma \frac{\Delta_Z}{2} + \zeta + \xi \beta \Delta_B. \quad (10)$$

At zero bias, the degeneracy of the octet of states in $N = 0$ is lifted by the Zeeman, the γ_4 and the δ_0 terms. These couplings are small however since

$$\zeta = 0.39 B [\text{T}] \text{ meV}, \quad (11)$$

$$\Delta_Z = 0.12 B [\text{T}] \text{ meV}. \quad (12)$$

In the simplest tight-binding model where $\gamma_4 = \delta_0 = 0$ and with $\Delta_Z = \Delta_B = 0$, the Landau level spectrum is given by $E_N = \text{sgn}(N) \sqrt{|N|(|N|+1)} \hbar \omega_c^*$ where $N = 0, \pm 1, \pm 2, \dots$ and sgn is the signum function. The gap between the first two Landau levels is $E_1 - E_0 \approx 37 \text{ meV}$. The two-component spinors for the levels $(\xi, \sigma, n = 0, 1)$ are independent of the spin index σ and given, in the common basis (A_2, B_1) , by

$$\psi_{\xi=+1,n,X}(\mathbf{r}) = \begin{pmatrix} h_{n,X}(\mathbf{r}) \\ 0 \end{pmatrix}, \quad (13)$$

$$\psi_{\xi=-1,n,X}(\mathbf{r}) = \begin{pmatrix} 0 \\ h_{n,X}(\mathbf{r}) \end{pmatrix}, \quad (14)$$

with the Landau-level wave functions in the Landau gauge $\mathbf{A} = (0, Bx, 0)$ given by

$$h_{n,X}(\mathbf{r}) = \frac{1}{\sqrt{L_y}} e^{-iXy/\ell^2} \varphi_n(x - X), \quad (15)$$

where X is the guiding-center index.

Crossings between some levels of $N = 0$ and $N = 1$ occur at bias $|\Delta_B| \approx 0.1 \text{ eV}$ for $B = 10 \text{ T}$ and $|\Delta_B| \approx 0.2 \text{ eV}$ for $B = 30 \text{ T}$. Above these biases, it is in principle not possible to neglect Landau-level mixing.¹⁸

The $T = 0 \text{ K}$ phase diagram of the chiral 2DEG in $N = 0$ has been derived in Ref. 3 in the two-component model and in the Hartree-Fock approximation for integer filling factors $\nu \in [-3, 3]$ as a function of the bias Δ_B . In the present work, we study in more detail the phase diagram for filling factor $\nu = 3$ which corresponds to the filling of seven sub-levels in $N = 0$. According to Ref. 3, this means that all four spin up states are filled as well as the two states $n = 0, 1$ with $\sigma = -1$ in valley K_+ . Considering all these states as inert, we are left with a simple two-level system consisting of the two orbital states $n = 0, 1$ in valley K_- with $\sigma = -1$. We denote by $\tilde{\nu}$ the filling factor of this two-level system so that $\tilde{\nu} = 1$ when $\nu = 3$. The order parameters of the different phases are given by

$$\begin{aligned} \langle \rho_{n,m}(\mathbf{q}) \rangle &= \frac{1}{N_\varphi} \sum_{X,X'} e^{-\frac{i}{2} q_x (X+X')} \\ &\times \left\langle c_{X,n}^\dagger c_{X',m} \right\rangle \delta_{X,X'+q_y \ell^2}, \end{aligned} \quad (16)$$

where N_φ is the Landau-level degeneracy and \mathbf{q} is a two-dimensional vector in the plane of the 2DEG. Hereafter, we drop the indices $\xi = -1, \sigma = -1$ to simplify the notation. The diagonal elements $\langle \rho_{n,n}(\mathbf{q} = 0) \rangle = \tilde{\nu}_n$ give the filling factor of each level n while the off-diagonal elements describe orbital coherence.

These average electronic density $n(\mathbf{q})$ is given by

$$n(\mathbf{q}) = N_\varphi \sum_{n,m} K_{n,m}(-\mathbf{q}) \langle \rho_{n,m}(\mathbf{q}) \rangle, \quad (17)$$

where the form factors

$$K_{0,0}(\mathbf{q}) = e^{\frac{-q^2 \ell^2}{4}}, \quad (18)$$

$$K_{1,1}(\mathbf{q}) = e^{\frac{-q^2 \ell^2}{4}} \left(1 - \frac{q^2 \ell^2}{2} \right), \quad (19)$$

$$K_{1,0}(\mathbf{q}) = e^{\frac{-q^2 \ell^2}{4}} \left(\frac{(q_y + i q_x) \ell}{\sqrt{2}} \right), \quad (20)$$

$$K_{0,1}(\mathbf{q}) = e^{\frac{-q^2 \ell^2}{4}} \left(\frac{(-q_y + i q_x) \ell}{\sqrt{2}} \right), \quad (21)$$

capture the orbital character of the two states.

In a pseudospin language, the states $n = 0, 1$ are represented by the up and down pseudospin states respectively. The orbital pseudospin vector $\mathbf{p}(\mathbf{q})$ is related to

the operators $\rho_{n,m}(\mathbf{q})$ by

$$\rho(\mathbf{q}) = \rho_{0,0}(\mathbf{q}) + \rho_{1,1}(\mathbf{q}), \quad (22)$$

$$p_x(\mathbf{q}) = [\rho_{0,1}(\mathbf{q}) + \rho_{1,0}(\mathbf{q})]/2, \quad (23)$$

$$p_y(\mathbf{q}) = [\rho_{0,1}(\mathbf{q}) - \rho_{1,0}(\mathbf{q})]/2i, \quad (24)$$

$$p_z(\mathbf{q}) = [\rho_{0,0}(\mathbf{q}) - \rho_{1,1}(\mathbf{q})]/2, \quad (25)$$

and $|\langle \mathbf{p}(0) \rangle| = 1/2$ for $\tilde{\nu} = 1$.

The phase diagram at $\tilde{\nu} = 1$ contains both uniform and nonuniform states with pseudospin textures. The Hartree-Fock energy for a state with a pseudospin texture is given by⁹ (apart from some unimportant constant terms) by

$$\begin{aligned} \frac{E_{HF}}{N} = & -\beta(\Delta_M - \Delta_B) \langle \tilde{p}_z(0) \rangle \\ & + \frac{1}{2} \left(\frac{e^2}{\kappa \ell} \right) \sum_{\mathbf{q}} \langle \tilde{\mathbf{p}}_{\parallel}(-\mathbf{q}) \rangle \cdot [a(\mathbf{q}) \mathbf{I} + b(\mathbf{q}) \mathbf{\Lambda}(\mathbf{q})] \cdot \langle \tilde{\mathbf{p}}_{\parallel}(\mathbf{q}) \rangle \\ & + \frac{1}{2} \left(\frac{e^2}{\kappa \ell} \right) \sum_{\mathbf{q}} c(\mathbf{q}) \langle \tilde{p}_z(-\mathbf{q}) \rangle \langle \tilde{p}_z(\mathbf{q}) \rangle \\ & + \frac{i}{4} \left(\frac{e^2}{\kappa \ell} \right) \sum_{\mathbf{q}} d(\mathbf{q}) (\hat{\mathbf{z}} \times \hat{\mathbf{q}}) \cdot [\langle \tilde{\mathbf{p}}(-\mathbf{q}) \rangle \times \langle \tilde{\mathbf{p}}(\mathbf{q}) \rangle], \end{aligned} \quad (26)$$

where $\tilde{\mathbf{p}} \equiv (-p_x, p_y, p_z)$, \mathbf{I} is the 2×2 unit tensor and

$$\mathbf{\Lambda}(\mathbf{q}) = \begin{pmatrix} \cos(2\varphi_{\mathbf{q}}) & \sin(2\varphi_{\mathbf{q}}) \\ \sin(2\varphi_{\mathbf{q}}) & -\cos(2\varphi_{\mathbf{q}}) \end{pmatrix}, \quad (27)$$

where $\varphi_{\mathbf{q}}$ is the angle between the wave vector \mathbf{q} and the x axis. The interactions $a(\mathbf{q})$, $b(\mathbf{q})$, $c(\mathbf{q})$ and $d(\mathbf{q})$ are defined in Ref. 9. The bias Δ_M defines the middle of the spiral phase in Fig. 1.

The interaction energy of the 2DEG with a uniform external electric field $\mathbf{E}_{\parallel} = -\nabla V(\mathbf{r})$ applied in the plane of the bilayer is given by

$$\begin{aligned} \langle H_{\mathbf{E}_{\parallel}} \rangle &= -e \int d\mathbf{r} n(\mathbf{r}) V(\mathbf{r}) \\ &= - \int d\mathbf{r} \mathbf{d}(\mathbf{r}) \cdot \mathbf{E}_{\parallel}, \end{aligned} \quad (28)$$

with the average density $n(\mathbf{r})$ defined in Eq. (17) and the average total electric dipole $\mathbf{d}(\mathbf{q})$ related to the pseudospin operator $\tilde{\mathbf{p}}$ by¹⁵

$$\mathbf{d}(\mathbf{q}) = \sqrt{2}e\ell N_{\varphi} e^{-\frac{q^2 \ell^2}{4}} \langle \tilde{\mathbf{p}}_{\parallel}(\mathbf{q}) \rangle. \quad (29)$$

To get Eq. (28), we have taken into account that, for all phases studied in this work, the condition $\langle \rho(\mathbf{q}) \rangle = \delta_{\mathbf{q},0}$ is satisfied.

III. PHASE DIAGRAM FOR $\tilde{\nu} = 1$

For $\mathbf{E}_{\parallel} = 0$, the sequence of ground states^{3,8,9} as the bias is increased is illustrated in Fig. 1. We use the values

$B = 10$ T and $\kappa = 5$ for the host dielectric constant in all our numerical calculations. The different phases are as follows:

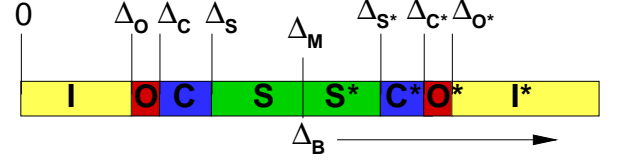


FIG. 1: (Color online) Phase diagram of the 2DEG in bilayer graphene at filling factor $\tilde{\nu} = 1$. The biases Δ_i indicate the onset of each phase. (The bias axis is not to scale.)

- Phase *I* for $\Delta_B \in [0, \Delta_O = \zeta/\beta]$ is a uniform phase where all pseudospins are oriented along $\hat{\mathbf{z}}$ (i.e. $\tilde{\nu}_0 = 1$). The Hartree-Fock gap (the energy to create an electron-hole pair) is given by $\Delta_{eh} = \eta/2 + \beta(\Delta_O - \Delta_B)$ and is shown in Fig. 5. Phase *I* has a pseudospin-wave mode with a dispersion $\omega_I(\mathbf{q})$, shown in Fig. 4(a), with a gap $\omega_I(0) = \beta(\Delta_O - \Delta_B)/\hbar$. This phase becomes unstable at $\Delta_O = \zeta/\beta$ which is the onset of the coherent phase *O*. The energy

$$\eta = \sqrt{\frac{\pi}{2}} \left(\frac{e^2}{\kappa \ell} \right) = \frac{56.1 \sqrt{B[\text{T}]}}{\kappa} \text{meV}. \quad (30)$$

- Phase *O* for $\Delta_B \in [\Delta_O, \Delta_C]$ is a uniform coherent phase where all the pseudospins are tilted by an angle θ with respect to the z axis with $\cos(\theta) = 1 - 8\beta(\Delta_B - \Delta_O)/\eta$. The Hartree-Fock gap $\Delta_{eh} = \eta/2$ is constant in this phase as shown by the dashed line in Fig. 5. The energy of this phase is invariant with respect to a collective rotation of the pseudospins around the z axis. It thus has a gapless pseudospin-wave mode whose dispersion, shown in Fig. 4(b), is highly anisotropic in the $x - y$ plane.⁸ Figure 4(b) shows the dispersion in the directions parallel (x) and perpendicular (y) to the dipoles when they are oriented in the $\hat{\mathbf{x}}$ direction. The origin of the orbital coherence is easy to understand. From Eqs. (9)-(10), $E_{n=1} > E_{n=0}$ at $\Delta_B = 0$ since $\zeta > 0$. As the bias is increased, however, $E_{n=1} \rightarrow E_{n=0}$ until $E_{n=1} \leq E_{n=0}$ above a critical bias $\Delta_B = \zeta/\beta$. The electrons should then occupy state $n = 1$ instead of $n = 0$. But, the Coulomb exchange energy is smaller when the electrons occupy level $n = 0$ instead of $n = 1$. To resolve this conflict, the system optimizes its energy by delocalizing the electrons in the two levels i.e. by creating a coherent state. When the small parameters γ_4, δ_0 are neglected, this coherence occurs at zero bias. The orbital coherence is associated with a finite electric polarization¹⁵ in the $x - y$ plane as shown in Eq. (29). Fluctuations of these dipoles are responsible for the electromagnetic absorption.

- Phase C for $\Delta_B \in [\Delta_C, \Delta_S]$ is a triangular Wigner crystal state with one electron per site and a vortex-like texture of pseudospins around each site as illustrated in Fig. 2. This texture is described by the Fourier components $\langle \mathbf{p}(\mathbf{G}) \rangle$, where $\{\mathbf{G}\}$ is the set of reciprocal lattice vectors of the crystal. The crystal has a gapless phonon mode, which has the characteristic long-wavelength dispersion $\omega \sim (q\ell)^{1.5}$ of a Wigner crystal in a magnetic field. There are also higher-energy gapped modes whose dispersions are shown in Fig. 4(c) and an electron-hole continuum of excitations.⁹ The Hartree-Fock gap Δ_{eh} for this phase is shown in Fig. 5.
- Phase S for $\Delta_B \in [\Delta_S, \Delta_{S^*}]$ is shown in Fig. 3. It is a spiral phase where the pseudospins rotate in the plane $z - n$ plane with $\hat{\mathbf{n}}$ being some arbitrary direction in the $x - y$ plane. The Fourier components $\langle \mathbf{p}(mQ\hat{\mathbf{n}}) \rangle \neq 0$, where $m = 0, \pm 1, \pm 2, \dots$ and Q is the wave vector of the spiral. The energy of the spiral is independent of the orientation of $\hat{\mathbf{n}}$ and so it has a gapless phonon mode. There are also higher-energy gapped mode whose dispersion are shown in Fig. 4(d) and an electron-hole continuum of excitations.⁹ The dispersion of these modes is highly anisotropic. The gap Δ_{eh} for this phase is shown in Fig. 5.

The phase diagram is symmetrical with respect to the bias $\Delta_M = \zeta/\beta + \eta/8\beta$ which is in the middle of the spiral phase. We say that a phase with $\Delta_B^{(2)} = \Delta_M + \Delta$ is the *conjugate* of that with $\Delta_B^{(1)} = \Delta_M - \Delta$ (with $\Delta > 0$) in the sense that it has the same gap Δ_{eh} and the same spectrum of collective modes. The filling factors $\tilde{\nu}_0 > \tilde{\nu}_1$ for $\Delta_B^{(1)}$ and vice versa for $\Delta_B^{(2)}$. We denote the conjugate phases with $\Delta_B > \Delta_M$ by S^*, C^*, O^*, I^* . In phase I^* , the pseudospin are aligned along $-\hat{\mathbf{z}}$ (i.e. $\tilde{\nu}_1 = 1$), the gap of the pseudospin-wave mode is given by $\omega_{I^*}(0) = \beta(\Delta_B - \Delta_{O^*})/\hbar$ and $\Delta_{eh} = \eta/2 + \beta(\Delta_B - \Delta_{O^*})$. The bias $\Delta_{O^*} = \zeta/\beta + \eta/4\beta$. There are no more phase transitions for $\Delta_B > \Delta_{O^*}$ in the two-level system.

With the hopping parameters given in Sec. II, the critical biases in meV are: $\Delta_O = 53.2$, $\Delta_C = 55.7$, $\Delta_S = 75.6$, $\Delta_{S^*} = 184.6$, $\Delta_M = 130.1$, $\Delta_{C^*} = 204.5$, $\Delta_{O^*} = 207.0$. Thus, at $B = 10$ T and $\kappa = 5$, only the first half of the phase diagram falls below the limits of validity of the two-component model. But, the full phase diagram should be visible at higher magnetic field. At $B = 30$ T, for example, $\Delta_{O^*} < 200$ meV which is within the limits of validity of the model.¹⁸

IV. EFFECT OF A PARALLEL ELECTRIC FIELD ON THE PHASE DIAGRAM

Adding the dipole term of Eq. (28) to the Hartree-Fock Hamiltonian and using the formalism described in

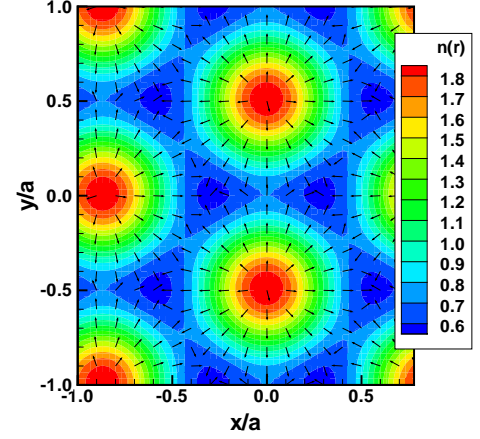


FIG. 2: (Color online) Electronic density $n(\mathbf{r})$ and dipole pattern (arrows) $\mathbf{d}(\mathbf{r})$ for the Wigner crystal phase at $\Delta_B = 59$ meV.

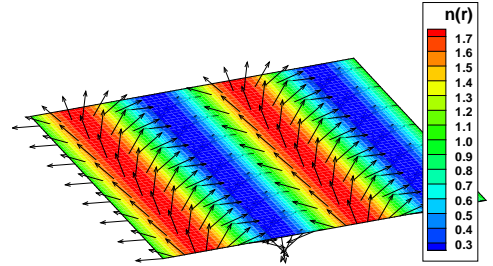


FIG. 3: (Color online) Electronic density $n(\mathbf{r})$. The arrows represent the dipole $\mathbf{d}(\mathbf{r})$ and pseudospin fields $\langle p_z(\mathbf{r}) \rangle$ of the spiral phase for $\Delta_B = 112$ meV.

Refs. 3,9 to compute the single-particle Green's function, we obtain the phase diagram shown in Fig. 6. With a finite parallel electric field \mathbf{E}_{\parallel} , the pseudospins are pushed towards the $x - y$ plane. The I and I^* phases are transformed into the O and O^* phases and orbital coherence is then always present. We find that the orientation of the wave vector \mathbf{Q} that minimizes the Hartree-Fock energy is $\mathbf{Q} \perp \mathbf{E}_{\parallel}$. From Fig. 6, it can be seen that, although a small electric field is sufficient to suppress the crystal phase, a much larger field is needed to destroy the spiral phase. This field is 0.30 mV/nm at $\Delta_B = 0.13$ eV in the middle of the spiral phase (not shown in the figure). The 2DEG is described by the pseudospin energy functional given in Eq. (26) where the effective pseudospin Heisenberg exchange interaction is highly anisotropic. Figure 7

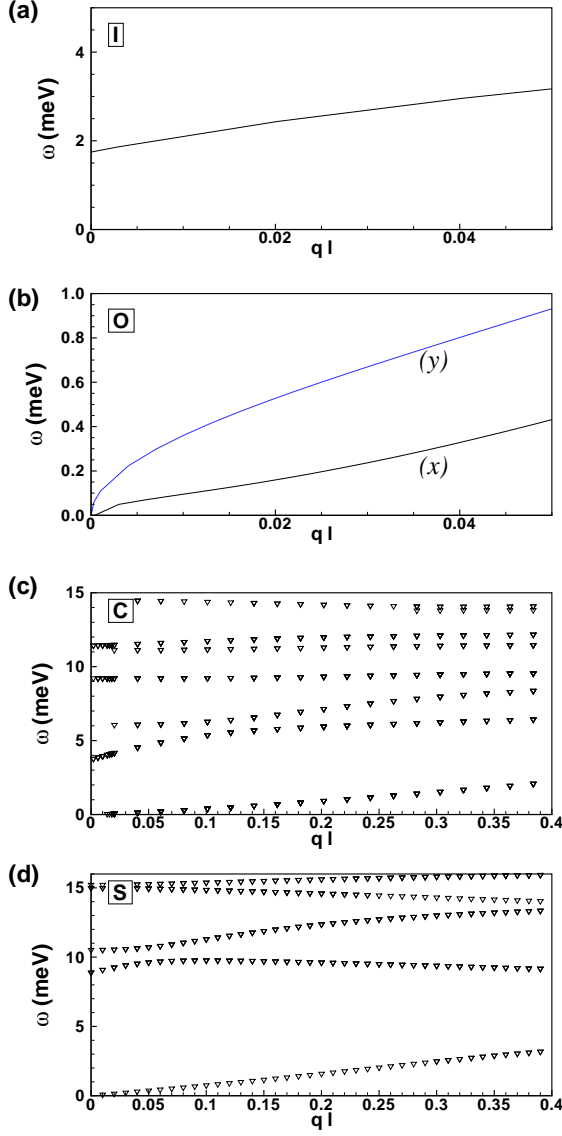


FIG. 4: (Color online) Dispersion relations for the (a) incoherent phase I at $\Delta_B = 29$ meV; (b) coherent phase O at $\Delta_B = 54$ meV; (c) crystal phase C at $\Delta_B = 66$ meV, and (d) spiral phase S at $\Delta_B = 77$ meV.

gives an idea of the strength of the parallel electric field which is necessary to tilt the pseudospin away from the z axis, against the interaction $c(q) < 0$ that tends to keep them aligned with that axis.

When $E_{\parallel} \neq 0$, the Hartree-Fock electron-hole gap is modified in the manner shown in Fig. 5. The gap is only slightly increased in the incoherent and coherent phases and does not change noticeably in the crystal and spiral phases for an electric field $E_{\parallel} = 0.04$ mV/nm which is near the upper-limit of the crystal phase in Fig. 6.

Figure 8 shows how the pseudospin-wave optical gaps $\omega_I(0)$ and $\omega_O(0)$ of the I and O phases change with bias for different values of the electric field. The electric field increases the optical gap in the incoherent phase I . In the

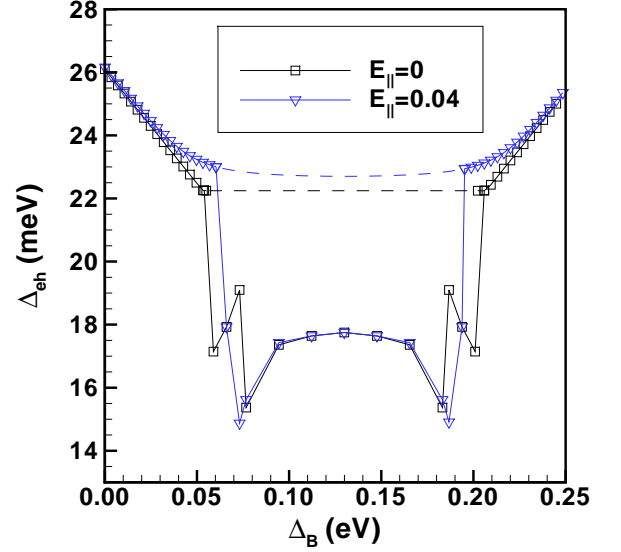


FIG. 5: (Color online) Hartree-Fock electron-hole gap Δ_{eh} as a function of bias for two values of the parallel electric field $\mathbf{E}_{\parallel} = E_{\parallel} \hat{x}$ in mV/nm. The dashed lines indicate the gap in the uniform coherent phase O when it is not the ground state. This phase is replaced by the crystal and spiral phases with smaller gap in most of the phase diagram.

coherent phase O , it destroys the $U(1)$ symmetry of the Hamiltonian thus gapping the Goldstone mode.¹⁵ The gap is practically constant in the small range of the O phase (the flat region of each curve in Fig. 5). Note that the optical gap $\omega_I(0) \rightarrow 0$ as $\Delta_B \rightarrow \Delta_O$ when $E_{\parallel} = 0$. As discussed below, electromagnetic absorption is expected at the gap frequency.

The dispersion at small wave vector in the crystal phase does not change very much for an electric field $E_{\parallel} = 0.04$ mV/nm. In the spiral phase, however, the field can be increased to a larger value and it is possible to modify noticeably the dispersion. In Fig. 9, $E_{\parallel} = 0$ and $E_{\parallel} = 0.15$ mV/nm and the dispersions are shown in the direction of the spiral. In both the crystal and spiral phases, the phonon mode is not gapped by a finite \mathbf{E}_{\parallel} . This is easily understood since the coupling to the external \mathbf{E}_{\parallel} involves the total electric dipole moment, a quantity that is not changed by a rigid translation of the system.

V. ELECTROMAGNETIC ABSORPTION FROM COLLECTIVE MODES

In this section, we give detailed derivation of the power absorbed $P(\omega)$ by the collective excitations in both the uniform and nonuniform phases following in parts Ref. 19 where $P(\omega)$ was calculated for collective modes in quantum wires. The average power per unit area absorbed

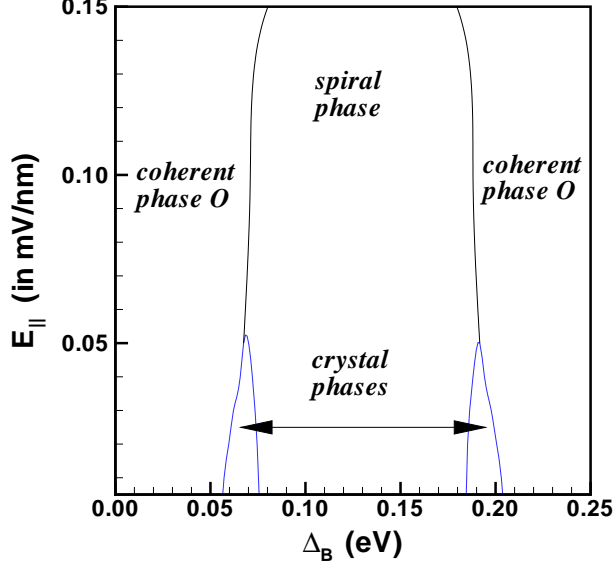


FIG. 6: (Color online) Phase diagram of the 2DEG as a function of the bias Δ_B and the electric field $E_{||}$.

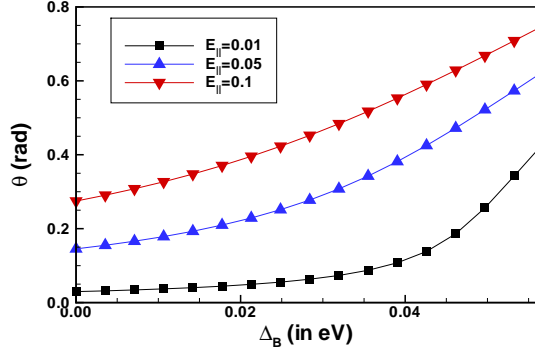


FIG. 7: (Color online) In phase I , a parallel electric field $E_{||}$ tilts the pseudospins towards the $x - y$ plane by an angle $\theta(\Delta_B, E_{||})$. The field $E_{||}$ in the legend is in mV/nm.

from an electromagnetic wave $\mathbf{E}_e(\mathbf{r}, z, t)$ by a sample of size S located in the $x - y$ plane at $z = 0$ is given by

$$P(\omega) = \frac{1}{2S^2} \sum_{\mathbf{q}} \text{Re} [(\mathbf{E}(\mathbf{q}, z = 0, \omega))^* \cdot \mathbf{j}(\mathbf{q}, \omega)], \quad (31)$$

where \mathbf{j} is the surface current density in the sample and \mathbf{E} is the *total* electric field within the sample. Since nonuniform as well as uniform phases must be considered, it is necessary to use the following general relation between the current density and the total electric field

$$\mathbf{j}(\mathbf{q}, \omega) = \sum_{\mathbf{q}'} \overleftrightarrow{\sigma}(\mathbf{q}, \mathbf{q}', \omega) \cdot \mathbf{E}(\mathbf{q}', z = 0, \omega), \quad (32)$$

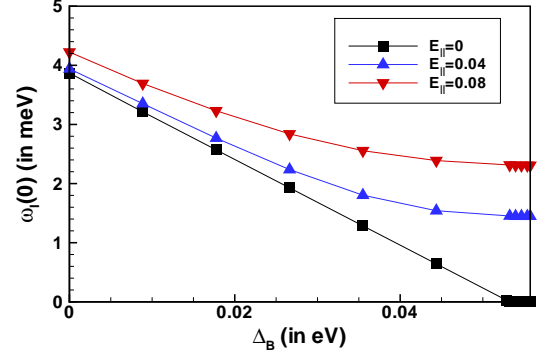


FIG. 8: (Color online) Optical gaps $\omega_I(0)$ and $\omega_O(0)$ as a function of bias for different values of the parallel electric field (in mV/nm). The flat region of each curve corresponds to the coherent phase O .

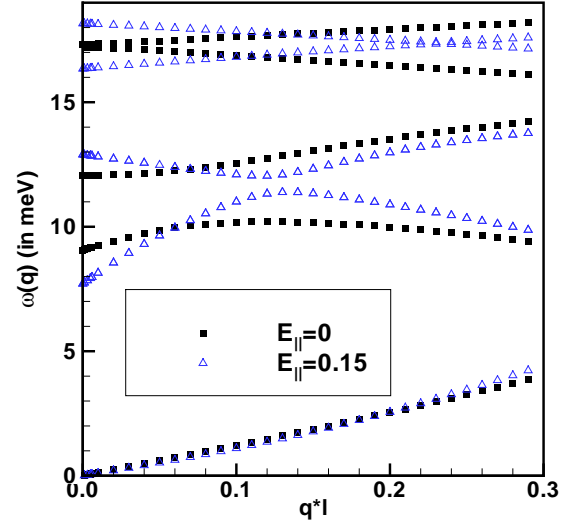


FIG. 9: (Color online) Dispersion relation of the collective modes in the direction of the spiral at bias $\Delta_B = 130$ meV for electric field strengths $E_{||} = 0$ and $E_{||} = 0.15$ mV/nm.

where $\overleftrightarrow{\sigma}$ is related to the irreducible or proper part of the two-dimensional current response function. Equation (32) can also be written as

$$\mathbf{j}(\mathbf{q}, \omega) = \sum_{\mathbf{q}'} \overleftrightarrow{\sigma}(\mathbf{q}, \mathbf{q}', \omega) \cdot \mathbf{E}_e(\mathbf{q}', z = 0, \omega), \quad (33)$$

where $\overleftrightarrow{\sigma}$ is now related to the full (i.e. screened) two-dimensional current response function. In our case, it is the current response computed in the generalized random-phase approximation (GRPA). In the above relations, \mathbf{q}, \mathbf{q}' and \mathbf{r} are two-dimensional vectors in the plane of the 2DEG. The absorbed power is thus

where the tensor

$$P(\omega) = \frac{1}{2S^2} \sum_{\mathbf{q}, \mathbf{q}'} \text{Re} [\mathbf{E}(\mathbf{q}, z=0, \omega)^* \cdot \overleftrightarrow{\sigma}(\mathbf{q}, \mathbf{q}', \omega) \cdot \mathbf{E}_e(\mathbf{q}', z=0, \omega)] \quad (34)$$

From Maxwell equations, the total and external electric fields \mathbf{E} and \mathbf{E}_e are related by

$$\mathbf{E}(\mathbf{q}, z, \omega) = \mathbf{E}_e(\mathbf{q}, z, \omega) - \frac{4\pi i}{\omega} \frac{1}{L} \sum_{q_z} \overleftrightarrow{K}(\mathbf{p}, \omega) \cdot e^{iq_z z} \sum_{\mathbf{q}'} \overleftrightarrow{\sigma}(\mathbf{q}, \mathbf{q}', \omega) \cdot \mathbf{E}_e(\mathbf{q}', z=0, \omega), \quad (35)$$

$$\overleftrightarrow{K}(\mathbf{p}, \omega) = \widehat{\mathbf{p}}\widehat{\mathbf{p}} + \frac{\omega^2}{\omega^2 - c^2 p^2} (\overleftrightarrow{1} - \widehat{\mathbf{p}}\widehat{\mathbf{p}}), \quad (36)$$

with $\mathbf{p} = (\mathbf{q}, q_z)$ and $\overleftrightarrow{1}$ the three-dimensional unit tensor.

The total electric field is given by

$$\begin{aligned} \mathbf{E}(\mathbf{q}, z, \omega) = & \mathbf{E}_e(\mathbf{q}, z, \omega) \\ & - \frac{4\pi i}{\omega} \frac{1}{L} \sum_{q_z} \frac{\omega^2 e^{iq_z z}}{\omega^2 - c^2 p^2} \sum_{\mathbf{q}'} \overleftrightarrow{\sigma}(\mathbf{q}, \mathbf{q}', \omega) \cdot \mathbf{E}_e(\mathbf{q}', z=0, \omega) \\ & + \frac{4\pi i}{\omega} \frac{1}{L} \sum_{q_z} \frac{c^2 e^{iq_z z}}{\omega^2 - c^2 p^2} \mathbf{p}\mathbf{p} \cdot \sum_{\mathbf{q}'} \overleftrightarrow{\sigma}(\mathbf{q}, \mathbf{q}', \omega) \cdot \mathbf{E}_e(\mathbf{q}', z=0, \omega) \end{aligned} \quad (37)$$

and the absorption by

$$\begin{aligned} P(\omega) = & \frac{1}{2S^2} \sum_{\mathbf{q}, \mathbf{q}'} \text{Re} [\mathbf{E}_e^*(\mathbf{q}, z=0, \omega) \cdot \overleftrightarrow{\sigma}(\mathbf{q}, \mathbf{q}', \omega) \cdot \mathbf{E}_e(\mathbf{q}', z=0, \omega)] \\ & - \frac{1}{2S^2} \sum_{\mathbf{q}} \text{Re} \left[\frac{4\pi i}{\omega} \frac{1}{L} \sum_{q_z} \frac{\omega^2}{\omega^2 - c^2 p^2} \right] \left| \sum_{\mathbf{q}'} \overleftrightarrow{\sigma}(\mathbf{q}, \mathbf{q}', \omega) \cdot \mathbf{E}_e(\mathbf{q}', z=0, \omega) \right|^2 \\ & + \frac{1}{2S^2} \sum_{\mathbf{q}} \text{Re} \left[\frac{4\pi i}{\omega} \frac{1}{L} \sum_{q_z} \frac{c^2}{\omega^2 - c^2 p^2} \right] \left| \sum_{\mathbf{q}'} \mathbf{p} \cdot \overleftrightarrow{\sigma}(\mathbf{q}, \mathbf{q}', \omega) \cdot \mathbf{E}_e(\mathbf{q}', z=0, \omega) \right|^2, \end{aligned} \quad (38)$$

where ω is short for $\omega + i\delta$.

In a crystal, translational symmetry imposes $\overleftrightarrow{\sigma}(\mathbf{q}, \mathbf{q}', \omega) \rightarrow \overleftrightarrow{\sigma}(\mathbf{k} + \mathbf{G}, \mathbf{k} + \mathbf{G}', \omega)$, where \mathbf{k} is a vector in the first Brillouin zone of the reciprocal lattice and \mathbf{G}, \mathbf{G}' are reciprocal lattice vectors. Thus, considering a plane electromagnetic wave $\mathbf{E}_e(\mathbf{q}, z=0, \omega) = SE_e \widehat{\mathbf{e}}_p \delta_{\mathbf{q}, 0}$ falling at normal incidence on the bilayer graphene system with polarisation vector $\widehat{\mathbf{e}}_p$, the absorption is:

$$\begin{aligned} P(\omega) = & \frac{E_e^2}{2} \text{Re} [\widehat{\mathbf{e}}_p^* \cdot \overleftrightarrow{\sigma}(0, 0, \omega) \cdot \widehat{\mathbf{e}}_p] \\ & - \frac{E_e^2}{2} \sum_{\mathbf{G}} \text{Re} \left[\frac{4\pi i}{\omega} \frac{1}{L} \sum_{q_z} \frac{\omega^2}{\omega^2 - c^2 q_z^2 - c^2 G^2} \right] |\overleftrightarrow{\sigma}(\mathbf{G}, 0, \omega) \cdot \widehat{\mathbf{e}}_p|^2 \\ & + \frac{E_e^2}{2} \sum_{\mathbf{G}} \text{Re} \left[\frac{4\pi i}{\omega} \frac{1}{L} \sum_{q_z} \frac{c^2 G^2}{\omega^2 - c^2 q_z^2 - c^2 G^2} \right] |\widehat{\mathbf{G}} \cdot \overleftrightarrow{\sigma}(\mathbf{G}, 0, \omega) \cdot \widehat{\mathbf{e}}_p|^2. \end{aligned} \quad (39)$$

The lattice constant in the crystal phase is $a_0 = 220 \text{ \AA}$ at $B = 10 \text{ T}$ (using the relation $2\pi n\ell^2 = \tilde{\nu} = 1$). It follows that the smallest reciprocal lattice vector $G \approx 10^8 \text{ m}^{-1}$ and the corresponding frequency $cG \approx 10^{16} \text{ rad/s}$. The frequency of the collective modes, on the other hand, is of order 10 meV i.e. $\approx 10^{13} \text{ rad/s}$. Thus, $\omega \ll cG$. Keeping terms to

order one in ω/cG , we get for the absorption

$$P(\omega) \approx \frac{E_e^2}{2} \text{Re} [\hat{\mathbf{e}}_p^* \cdot \overleftrightarrow{\sigma}(0, 0, \omega) \cdot \hat{\mathbf{e}}_p] + \frac{E_e^2}{2} \sum_{\mathbf{G} \neq 0} \text{Re} \left[\frac{2\pi i}{c} \left(\frac{\omega}{cG} \right) \right] |\overleftrightarrow{\sigma}(\mathbf{G}, 0, \omega) \cdot \hat{\mathbf{e}}_p|^2 - \frac{E_e^2 \pi}{c} |\overleftrightarrow{\sigma}(0, 0, \omega) \cdot \hat{\mathbf{e}}_p|^2 - \frac{E_e^2}{2} \sum_{\mathbf{G}} \text{Re} \left[\frac{2\pi i}{\omega} \right] |\mathbf{G} \cdot \overleftrightarrow{\sigma}(\mathbf{G}, 0, \omega) \cdot \hat{\mathbf{e}}_p|^2. \quad (40)$$

The only contributions at $\omega \neq 0$ come from the first and third terms on the right-hand side of Eq. (40). Defining

$$\overleftrightarrow{\sigma}(0, 0, \omega) = \frac{e^2}{h} \overleftrightarrow{\sigma}(\omega), \quad (41)$$

we have

$$P(\omega \neq 0) \approx \frac{e^2 E_e^2}{2h} \text{Re} [\hat{\mathbf{e}}_p^* \cdot \overleftrightarrow{\sigma}(\omega) \cdot \hat{\mathbf{e}}_p] - \alpha \frac{e^2 E_e^2}{2h} |\overleftrightarrow{\sigma}(\omega) \cdot \hat{\mathbf{e}}_p|^2, \quad (42)$$

where $\alpha = e^2/\hbar c = 1/137$ is the fine-structure constant and $\overleftrightarrow{\sigma}(\omega)$ is now unitless. For realistic values of δ , the condition $\alpha \overleftrightarrow{\sigma}(\omega) \ll 1$ is satisfied and the second term in the right-hand side of Eq. (42) can be neglected. The approximations that we have made to get Eq. (42) are equivalent to neglecting retardation effects [i.e. to taking the limit $c \rightarrow \infty$ in Eq. (39)]. In fact, since retardation effects are neglected in the GRPA for the conductivity, it seems logical to neglect them also in the calculation of the absorption. We have finally at finite frequency

$$P(\omega) = \frac{e^2 E_e^2}{2h} \text{Re} [\hat{\mathbf{e}}_p^* \cdot \overleftrightarrow{\sigma}(\omega) \cdot \hat{\mathbf{e}}_p]. \quad (43)$$

We take the incoming wave to be circularly polarized so that $\hat{\mathbf{e}}_p \rightarrow \hat{\mathbf{e}}_{\pm} = (\hat{\mathbf{x}} \pm i\hat{\mathbf{y}})/\sqrt{2}$ and the absorption is, from Eq. (43),

$$P_{\pm}(\omega) = \frac{e^2 E_e^2}{2h} \text{Re} [\sigma_{\pm}(\omega)], \quad (44)$$

where the conductivities σ_{\pm} are defined by

$$\sigma_{\pm} \equiv \sigma_{x,x} + \sigma_{y,y} \pm i\sigma_{x,y} \mp i\sigma_{y,x}. \quad (45)$$

Now, the optical conductivity is related to the current response $\Xi_{\alpha,\beta}(\tau) \equiv -\frac{1}{\hbar S} \langle T J_{\alpha}(\tau) J_{\beta}(0) \rangle$ by

$$\text{Re}[\sigma_{i,i}(\omega)] = -\frac{\text{Im}[\Xi_{i,i}(\omega)]}{\omega}, \quad (46)$$

$$\text{Im}[\sigma_{i,i}(\omega)] = \frac{\text{Re}[\Xi_{i,i}(\omega) - \Xi_{i,i}(0)]}{\omega}, \quad (47)$$

and, for $i \neq j$, by

$$\sigma_{i,j}(\omega) = \frac{i}{(\omega + i\delta)} \Xi_{i,j}(\omega) \quad (48)$$

so that, for $\omega \neq 0$ and $i \neq j$, we have

$$\text{Re}[\sigma_{i,j}(\omega)] = -\frac{\text{Im}[\Xi_{i,j}(\omega)]}{\omega}, \quad (49)$$

$$\text{Im}[\sigma_{i,j}(\omega)] = \frac{\text{Re}[\Xi_{i,j}(\omega)]}{\omega}. \quad (50)$$

The total current operator is defined by $\mathbf{J} = -c \partial H^0 / \partial \mathbf{A}^e|_{\mathbf{A}^e=0}$, where H^0 is the non-interacting Hamiltonian of Eq. (1) where a Peierls substitution has been made to take into account an external electromagnetic field. In the two-component model, this current operator is related to the pseudospin operator by

$$J_{\alpha}(\tau) = -\frac{\sqrt{2}e\ell N_{\varphi}}{\hbar} (\zeta - \beta\Delta_B) p_{\bar{\alpha}}(\tau), \quad (51)$$

with the convention that $\bar{\alpha} = x$ if $\alpha = y$ and *vice versa* and with $p_{\alpha}(\tau) = p_{\alpha}(\mathbf{q} = 0, \tau)$. The two-particle current Matsubara Green's function tensor $\Xi_{\alpha,\beta}$ evaluated at $\mathbf{q} = 0$ can be related to the two-particle pseudospin Matsubara Green's function tensor $K_{\alpha,\beta}(\tau) = -\frac{N_{\varphi}}{\hbar} \langle T p_{\alpha}(\tau) p_{\beta}(0) \rangle$ by

$$\begin{aligned} \Xi_{\alpha,\beta}(\tau) &\equiv -\frac{1}{\hbar S} \langle T J_{\alpha}(\tau) J_{\beta}(0) \rangle \\ &= \frac{e^2}{\pi \hbar^2} (\zeta - \beta\Delta_B)^2 \left[-\frac{N_{\varphi}}{\hbar} \langle T p_{\bar{\alpha}}(\tau) p_{\bar{\beta}}(0) \rangle \right] \\ &\equiv \frac{e^2}{\pi \hbar^2} (\zeta - \beta\Delta_B)^2 K_{\bar{\alpha},\bar{\beta}}(\tau). \end{aligned} \quad (52)$$

Finally, $K_{\alpha,\beta}(\tau)$ can easily be related to the two-particle Green's functions defined with the operators in Eq. (16) i.e.

$$\chi_{n_1 n_2 n_3 n_4}(\tau) = -\frac{N_\varphi}{\hbar} \langle T \rho_{n_1, n_2}(\tau) \rho_{n_3, n_4}(0) \rangle \quad (53)$$

$$+\frac{N_\varphi}{\hbar} \langle \rho_{n_1, n_2} \rangle \langle \rho_{n_3, n_4} \rangle$$

by the equations

$$K_{x,x} = \frac{1}{4} [\chi_{++} + \chi_{+-} + \chi_{-+} + \chi_{--}], \quad (54)$$

$$K_{y,y} = -\frac{1}{4} [\chi_{++} - \chi_{+-} - \chi_{-+} + \chi_{--}], \quad (55)$$

$$K_{x,y} = \frac{1}{4i} [\chi_{++} - \chi_{+-} + \chi_{-+} - \chi_{--}], \quad (56)$$

$$K_{y,x} = \frac{1}{4i} [\chi_{++} + \chi_{+-} - \chi_{-+} - \chi_{--}], \quad (57)$$

where, to shorten the notation, we have defined the associations $+\equiv 01$ and $-\equiv 10$.

The current response is not isotropic in all phases so that $K_{x,x} \neq K_{y,y}$ in general. For the conductivities at $\mathbf{q} = 0$,

$$\text{Re}[\sigma_+(\omega)] = -\frac{e^2}{h} \frac{(\zeta - \beta\Delta_B)^2}{\hbar\omega} \text{Im}[\chi_{+-}(\omega)], \quad (58)$$

$$\text{Re}[\sigma_-(\omega)] = -\frac{e^2}{h} \frac{(\zeta - \beta\Delta_B)^2}{\hbar\omega} \text{Im}[\chi_{-+}(\omega)], \quad (59)$$

and for the absorption per unit area

$$P_+(\omega) = -\frac{e^2 E_e^2}{2h} \frac{(\zeta - \beta\Delta_B)^2}{\hbar\omega} \text{Im}[\chi_{+-}(\omega)], \quad (60)$$

$$P_-(\omega) = -\frac{e^2 E_e^2}{2h} \frac{(\zeta - \beta\Delta_B)^2}{\hbar\omega} \text{Im}[\chi_{-+}(\omega)]. \quad (61)$$

For linear polarizations, the absorption is given by

$$P_x(\omega) = \frac{e^2 E_e^2}{2h} \frac{(\zeta - \beta\Delta_B)^2}{\hbar\omega} \times \text{Im}[\chi_{++}(\omega) - \chi_{+-}(\omega) - \chi_{-+}(\omega) + \chi_{--}(\omega)], \quad (62)$$

$$P_y(\omega) = -\frac{e^2 E_e^2}{2h} \frac{(\zeta - \beta\Delta_B)^2}{\hbar\omega} \times \text{Im}[\chi_{++}(\omega) + \chi_{+-}(\omega) + \chi_{-+}(\omega) + \chi_{--}(\omega)], \quad (63)$$

for an electric field polarized in the $\hat{\mathbf{x}}$ or $\hat{\mathbf{y}}$ direction respectively.

A. Incoherent phases I and I^*

Analytical expressions for the absorption are possible in the incoherent phases when the parallel electric field $\mathbf{E}_\parallel = 0$. Using the results derived in Ref. 3, the only two non-zero GRPA response functions at $\mathbf{q} = 0$ in these phases are $\chi_{+-}(\omega)$ and $\chi_{-+}(\omega)$ with

$$\chi_{\mp\pm}(\omega) = \pm \frac{\nu_1 - \nu_0}{\hbar\omega + i\delta \pm (\zeta - \beta\Delta_B + \frac{1}{4}\eta\nu_1)}. \quad (64)$$

For phases I and I^* , the absorption is given by

$$P_\pm^{(I)}(\omega) = \frac{e^2 E_e^2}{2h} \frac{\pi}{\hbar} \beta (\Delta_O - \Delta_B) \delta(\omega \mp \omega_I(0)), \quad (65)$$

$$P_\pm^{(I^*)}(\omega) = \frac{e^2 E_e^2}{2h} \frac{\pi}{\hbar} \beta \frac{(\Delta_B - \Delta_O)^2}{(\Delta_B - \Delta_{O^*})} \delta(\omega \pm \omega_{I^*}(0)) \quad (66)$$

where the frequencies $\omega_I(0)$ (plotted in Fig. 8) and $\omega_{I^*}(0)$ have been defined in Sec. III. We remark that, from Eq. (64), it is clear that there is no contribution from the bubble (or polarization) diagrams in $\chi_{\mp\pm}(\omega)$ so that $\overleftrightarrow{\sigma}(0,0,\omega) = \overleftrightarrow{\sigma}^T(0,0,\omega)$ in these phases. This is not true in the nonuniform phases however.

The pseudospin-wave mode in these phases is circularly polarized. It shows up *only* in $P_+(\omega)$ for the I phase and *only* in $P_-(\omega)$ for the I^* phase. The response functions $\chi_{+-}(\omega)$ and $\chi_{-+}(\omega)$ are equal for conjugate phases, but because of the prefactor in Eqs. (60)-(61), the intensity of the absorption is not. The absorption $P_+(\omega)$ decreases as $\Delta_B \rightarrow \Delta_O$ in the I phase while $P_-(\omega)$ diverges (in the absence of disorder) at the $O^* \rightarrow I^*$ transition, decreases as the bias is increased and then increases linearly with Δ_B at still larger bias.

The maximal value of the absorption frequency $\omega_I(0)$ is at $\Delta_B = 0$ where $\hbar\omega_I(0) = 3.85$ meV i.e. $\nu_I(0) = 9.3 \times 10^{11}$ Hz in the far infrared. This frequency can be tuned all the way to zero by increasing Δ_B . It can also be increased by a finite \mathbf{E}_\parallel as shown in Fig. 8. With a finite \mathbf{E}_\parallel , the absorption still appears predominantly in $P_+(\omega)$ for phase I and in $P_-(\omega)$ for phase I^* , but the other circular component makes a very small contribution in each case.

B. Coherent phases O and O^*

In the coherent phases O and O^* , the pseudospin mode is gapless and there is no absorption at finite frequency. As shown in Fig. 6, a finite \mathbf{E}_\parallel gaps that mode and makes it visible in absorption. The range in bias where these two phases are the ground state is so small that the optical frequency can't change much with bias. The absorption is predominantly in $P_+(\omega)$ for $\Delta_B < \Delta_M$ and in $P_-(\omega)$ for $\Delta_B > \Delta_M$ but there is a small intensity in the other circular polarization which is smaller by a factor ≈ 10 .

C. Crystal phases C and C^*

Figure 10 shows the absorptions $P_\pm(\omega)$ in the conjugate crystal phases C [Fig. 10(a),(b)] and C^* [Fig. 10(c),(d)] at $\Delta_B = 66$ meV and $\Delta_B^* = 193.8$ meV with $E_\parallel = 0$ and $E_\parallel = 0.04$ mV/nm. This figure should be compared with Fig. 4 (c) where the dispersion of the collective modes of the crystal is plotted. The gapless phonon mode is absent of the spectrum for $\omega > 0$. As in the I and I^* phase, the modes active in $P_+(\omega)$ for $\Delta_B < \Delta_M$ are those active in $P_-(\omega)$ for $\Delta_B > \Delta_M$ and

vice versa. The absorption peaks are more intense when $\Delta_B > \Delta_M$ however. For $\Delta_B < \Delta_M$, the first gapped mode is seen only in $P_+(\omega)$ while the fourth one is seen only in $P_-(\omega)$ and is more than ten times smaller in intensity. The second and third modes are not active in $P_\pm(\omega)$ or $P_{x,y}(\omega)$ (not shown in the figure) for $E_\parallel = 0$. A finite E_\parallel activates the second and third modes but they get a very small intensity: the second mode is then active in $P_-(\omega)$ only while the third mode, showing up in both polarizations, seems to be linearly polarized. The energy of the dominant mode is $\hbar\omega \approx 4$ meV i.e. similar to the energy of the pseudospin mode at zero bias in the I phase. A parallel electric field does not change noticeably the frequency as we noted before. A linearly polarized electromagnetic wave excites all modes of $P_+(\omega)$ and $P_-(\omega)$. In the crystal phases, we have checked that the absorption $P_x(\omega) = P_y(\omega)$.

D. Spiral phase

Figure 1 shows the absorptions $P_\pm(\omega)$ in the spiral phase at conjugate biases $\Delta_B = 77$ meV [Fig. 11(a),(b)] and $\Delta_B^* = 183$ meV [Fig. 11(c),(d)] with and without electric field $E_\parallel = 0.04$ mV/nm. This figure should be compared with Fig. 4 (d) where the collective modes of the spiral are plotted. The gapless phonon mode is absent of the spectrum for $\omega > 0$. The spectrum has the same symmetry in $P_\pm(\omega)$ as in the crystal phases. For $\Delta_B < \Delta_M$, the first gapped mode is seen predominantly in $P_+(\omega)$ while the almost degenerate third and fourth gapped mode are more active in $P_-(\omega)$. In contrast with the crystal phase, however, the modes of the spiral are not fully circularly polarized since the first(third/fourth) mode is only about 5 times stronger(weaker) in $P_+(\omega)$ than in $P_-(\omega)$. In linear polarization (not shown in Fig. 4), both modes are stronger in $P_y(\omega)$ than in $P_x(\omega)$. Note that the spiral rotates in the $z-x$ plane for $E_\parallel = 0$ and the absorption is maximal when the electric field of the electromagnetic field is perpendicular to the spiral i.e. in $P_y(\omega)$, a fact already mentioned in Ref. 9. The energy of the most intense mode is ≈ 9 meV, slightly higher than in the crystal. At $\Delta_B = \Delta_M$, the two most active modes are fully linearly polarized: the first in y and the second in x as shown in Fig. 11(e). Thus, these two modes become more linearly polarized as $\Delta_B \rightarrow \Delta_M$ from above or from below.

The second mode is not active in absorption when $E_\parallel = 0$ but is activated when $E_\parallel \neq 0$. With a finite E_\parallel , the degeneracy of the third and fourth modes is lifted and they become active in absorption. The second mode is fully linearly polarized and appears in $P_y(\omega)$.

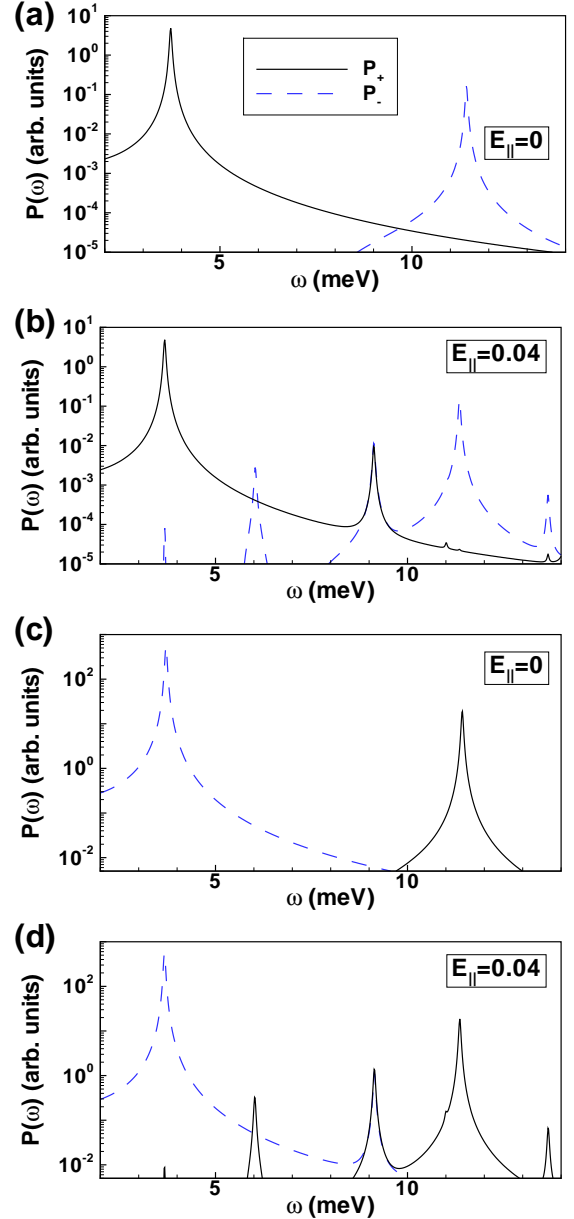


FIG. 10: (Color online) Absorptions $P_\pm(\omega)$ in the crystal phases C at $\Delta_B = 66$ meV [(a) and (b)] and C^* at the conjugate bias $\Delta_B = 194$ meV [(c) and (d)] with and without a parallel electric field $E_\parallel = 0.04$ mV/nm.

VI. KERR ROTATION FROM COLLECTIVE MODES

We adapt the calculation of Ref. 13 (see Supplemental material of this reference) to our specific problem to compute the Kerr angle for a graphene bilayer on top of a dielectric with a refractive index n_2 . We do not assume that $\sigma_{xx}(\omega) = \sigma_{yy}(\omega)$ since this symmetry is not satisfied in all phases and do not make the simplifying assumptions $\frac{4\pi}{c}\sigma_{xx}(\omega) \ll 1$, $\frac{4\pi}{c}\sigma_{xy}(\omega) \ll 1$. We take the incident wave \mathbf{E}_I in the medium 1 (the vacuum) to

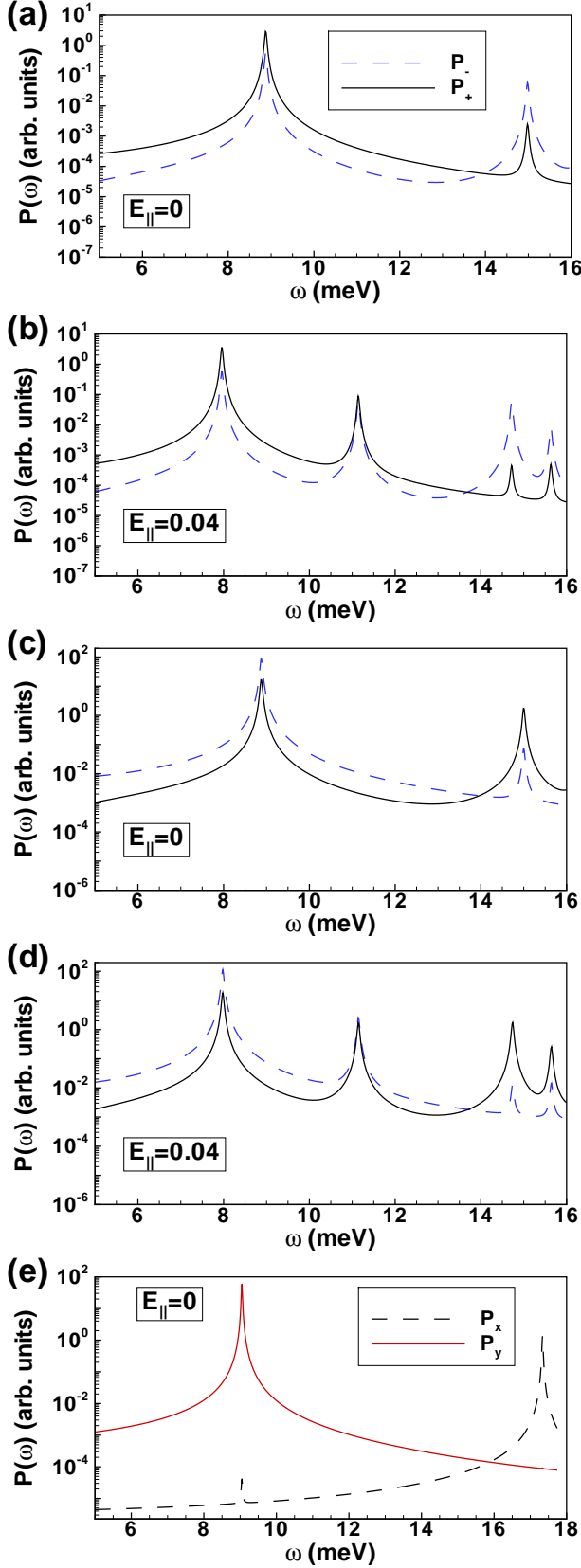


FIG. 11: (Color online) Absorptions $P_{\pm}(\omega)$ in the spiral phases at conjugate biases $\Delta_B = 77$ meV [(a) and (b)] and $\Delta_B = 183$ meV [(c) and (d)] with and without a parallel electric field $E_{\parallel} = 0.04$ mV/nm. (e) Absorption at bias $\Delta_M = 130$ meV and for $E_{\parallel} = 0$.

be linearly polarized. We write for the incident, reflected and transmitted (in medium 2) waves

$$\mathbf{E}_I = E_I \hat{\mathbf{x}} e^{i(k_1 z - \omega t)}, \quad (67)$$

$$\mathbf{E}_R = E_I (r_{xx} \hat{\mathbf{x}} + r_{yx} \hat{\mathbf{y}}) e^{i(-k_1 z - \omega t)}, \quad (68)$$

$$\mathbf{E}_T = E_I (t_{xx} \hat{\mathbf{x}} + t_{yx} \hat{\mathbf{y}}) e^{i(k_2 z - \omega t)}, \quad (69)$$

and for the corresponding magnetic fields

$$\mathbf{B}_I = \hat{\mathbf{z}} \times \mathbf{E}_I = E_I \hat{\mathbf{y}} e^{i(k_1 z - \omega t)}, \quad (70)$$

$$\mathbf{B}_R = -\hat{\mathbf{z}} \times \mathbf{E}_R = E_I (-r_{xx} \hat{\mathbf{y}} + r_{yx} \hat{\mathbf{x}}) e^{i(-k_1 z - \omega t)}, \quad (71)$$

$$\mathbf{B}_T = n_2 \hat{\mathbf{z}} \times \mathbf{E}_T = n_2 E_I (t_{xx} \hat{\mathbf{y}} - t_{yx} \hat{\mathbf{x}}) e^{i(k_2 z - \omega t)}, \quad (72)$$

with $k_1 = \omega/c$ and $k_2 = \omega n_2/c$. The wave arrives at normal incidence on the bilayer graphene and is in part reflected in medium 1 and in part transmitted to medium 2.

The boundary condition $\mathbf{E}_2^{\parallel} = \mathbf{E}_1^{\parallel}$ gives the equation

$$E_I \hat{\mathbf{x}} + E_I (r_{xx} \hat{\mathbf{x}} + r_{yx} \hat{\mathbf{y}}) = E_I (t_{xx} \hat{\mathbf{x}} + t_{yx} \hat{\mathbf{y}}), \quad (73)$$

while the boundary condition (the system is non-magnetic so that we take $\mathbf{B} = \mathbf{H}$) $\mathbf{B}_2^{\parallel} - \mathbf{B}_1^{\parallel} = \frac{4\pi}{c} \mathbf{j} \times \hat{\mathbf{z}}$ gives

$$\begin{aligned} & n_2 E_I (t_{xx} \hat{\mathbf{y}} - t_{yx} \hat{\mathbf{x}}) - E_I \hat{\mathbf{y}} + E_I (r_{xx} \hat{\mathbf{y}} - r_{yx} \hat{\mathbf{x}}) \\ &= \frac{4\pi}{c} (j_y \hat{\mathbf{x}} - j_x \hat{\mathbf{y}}), \end{aligned}$$

where \mathbf{j} is the induced surface current in the graphene bilayer. Now, according to our definition of the screened conductivity in Eq. (33), we must take

$$\mathbf{j}(\omega) = \frac{e^2}{h} \overleftrightarrow{\sigma}(\omega) \cdot \mathbf{E}_I(z=0, \omega), \quad (75)$$

where $\overleftrightarrow{\sigma}(\omega)$ is defined in Eq. (41). We implicitly assumed in the above derivation that, in the crystal and spiral phases, we can neglect the reent components $\{\mathbf{j}(\mathbf{G}, \omega)\}$ and keep only $\mathbf{j}(\omega) \equiv \mathbf{j}(\mathbf{G} = \mathbf{0}, \omega)$ and neglect the diffracted components in the electric field as well.

Solving Eqs. (74,73), we find for the Kerr (counter-clockwise) rotation angle from the x axis:

$$\tan(\theta_K) = \text{Re} \left(\frac{r_{yx}}{r_{xx}} \right) \quad (76)$$

$$= 2\alpha \text{Re} \left[\frac{\sigma_{yx}(\omega)}{n_2 - 1 + 2\alpha \sigma_{xx}(\omega)} \right]$$

where α is the fine-structure constant. For an incident wave polarized along the y axis, the (clockwise) rotation angle is obtained by the substitution $\sigma_{xx} \rightarrow \sigma_{yy}$ in the denominator of Eq. (76).

Figure 12 shows the Kerr angle $\theta_K(\omega)$ for $\Delta_B = 0$ in the I phase and for its conjugate bias $\Delta_B = 260$ meV in the I^* phase. We take $n_2 = \sqrt{5}$ and $E_{\parallel} = 0$. The Kerr effect occurs at the frequency of the collective mode

which is the same for both biases but the sense of rotation is opposite in the two phases. The rotation in the I^* phase takes place in a larger domain of frequencies (i.e. it is slower) than in the I phase and the maximum Kerr angle is also bigger. This is due to the prefactor $(\zeta - \beta\Delta_B)^2$ in the equation for the conductivity which makes the conductivities much larger in phase I^* and increases the contribution of $\sigma_{xx}(\omega)$ in the denominator of Eq. (76).

The maximal Kerr angle is large in Fig. 12 because we have taken a very small value for δ i.e. $\delta = 0.014$ meV. For $\delta = 0.14$ meV, the maximum angle for $\Delta_B = 0$ is reduced to 4.3 degrees which is of the order of the Kerr angle found for other types of broken-symmetry states studied before.¹⁴ For $\delta = 1.4$ meV, it is reduced to 0.7 degrees. Since δ approximates the effect of disorder, we see that the maximum Kerr angle is very sensitive to this parameter.

We remark that conductivity $\sigma_{xy}(\omega)$ should satisfy the condition $\text{Re}[\sigma_{xy}(\omega = 0)] = -1$ in the two-level system since $\tilde{\nu} = 1$. This condition is actually satisfied in phase I only and not in all the other phases. Indeed, Eq. (64) gives

$$\lim_{\delta \rightarrow 0} \sigma_{xy}^{(I)}(0) = -1, \quad (77)$$

$$\lim_{\delta \rightarrow 0} \sigma_{xy}^{(I^*)}(0) = \frac{(\Delta_B - \Delta_O)^2}{(\Delta_B - \Delta_{O^*})^2}. \quad (78)$$

We have verified that, when levels $|N| > 0$ are included in the calculation (in the four-component model and in the absence of interaction), the condition $\text{Re}[\sigma_{xy}(\omega = 0)] = -3$ is then satisfied ($\tilde{\nu} = 1 \Rightarrow \nu = 3$). The transitions from the levels $N \neq 0$ occur at higher frequencies, however, and they should not affect much the behavior of the Kerr rotation near a collective mode resonance a finite frequency.

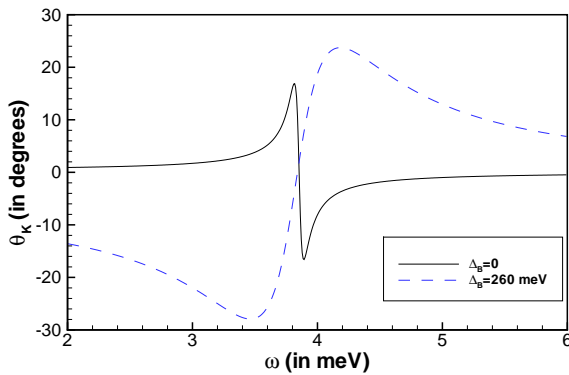


FIG. 12: (Color online) Kerr angle for conjugate biases $\Delta_B = 0$ and $\Delta_B = 260$ meV in the I and I^* phases.

Figure 13 shows the Kerr angle in the crystal and spiral phases for conjugate biases: (a) $\Delta_B = 66$ meV and (b) $\Delta_B = 194$ meV in the crystal phase and (c) $\Delta_B = 77$ meV and (d) $\Delta_B = 183$ meV in the spiral phase. We

take $n_2 = \sqrt{5}$ and $E_{\parallel} = 0$. As in phase I and I^* discussed above, our calculation does not include disorder so that we cannot get a quantitative result for the Kerr angle. We use $\delta \approx 0.014$ meV in all curves in this figure and use the same step in frequency so that we can compare the relative size of the rotation angle. As in Fig. 12, we expect that if disorder is included, it will reduce the Kerr angle. The modes visible in the Kerr rotation are also those active in absorption as can be seen by comparing Fig. 13 with Figs. 10-11. In the crystal and spiral phases where two modes are active in the range of frequency shown in Fig. 12, the Kerr angle for $\Delta_B < \Delta_M$ increases in going towards the resonance in the lower-energy mode while it decreases when approaching the fourth mode (the second and third mode do not appear in the Kerr rotation). The rotations are in the opposite directions for the conjugate biases. The Kerr rotation is bigger by a factor ≈ 10 in the conjugate phases with $\Delta_B > \Delta_M$. Since the same mode leads to opposite rotation of the polarization in for conjugate biases, the rotation must cease at bias Δ_M . We have checked numerically that this is the case.

In all phases but the spiral phase, we get numerically that the Kerr angle is the same for an incident wave polarized along the x or y axis. This is also true at small bias ($\Delta_B < \Delta_M$) in the spiral phase: a y polarization gives the same result as in Fig. 13 (c). For $\Delta_B > \Delta_M$, however, the rotation angle is bigger when the polarization is along the x axis (i.e. for a spiral rotating in the $z-x$ plane) as can be seen by comparing Fig. 13 (d) and Fig. 13 (e).

VII. CONCLUSION

We have continued in this work an analysis of a sequence of phase transitions involving uniform and nonuniform states with orbital coherence initiated in Ref. 9. This sequence, represented in Fig. 1, occurs at filling factor $\nu = 3$ of bilayer graphene, in Landau level $N = 0$, when an electric bias between the two levels is increased. At filling factor $\nu = 1$, the same states are found in the phase diagram but others involving spin coherence are present as well. In this work, we choose to concentrate on the simpler case of $\nu = 3$ in order to simplify the discussion but the same results would apply to the corresponding states at $\nu = 1$.

Because we were only interested in studying the signature of the collective excitations due to transitions between the two levels $n = 0, 1$ in Landau level $N = 0$, we could use the two-component model¹⁶ to simplify the calculations instead of working with the full four band model of bilayer graphene. All calculations were done at $T = 0$ K using the Hartree-Fock approximation to derive the phase diagram of the interacting chiral electron gas and the generalized random-phase approximation (GRPA) to obtain the dispersion relations of the collective modes.

Our calculations show that there are qualitative differences in the transport gap and in the optical properties

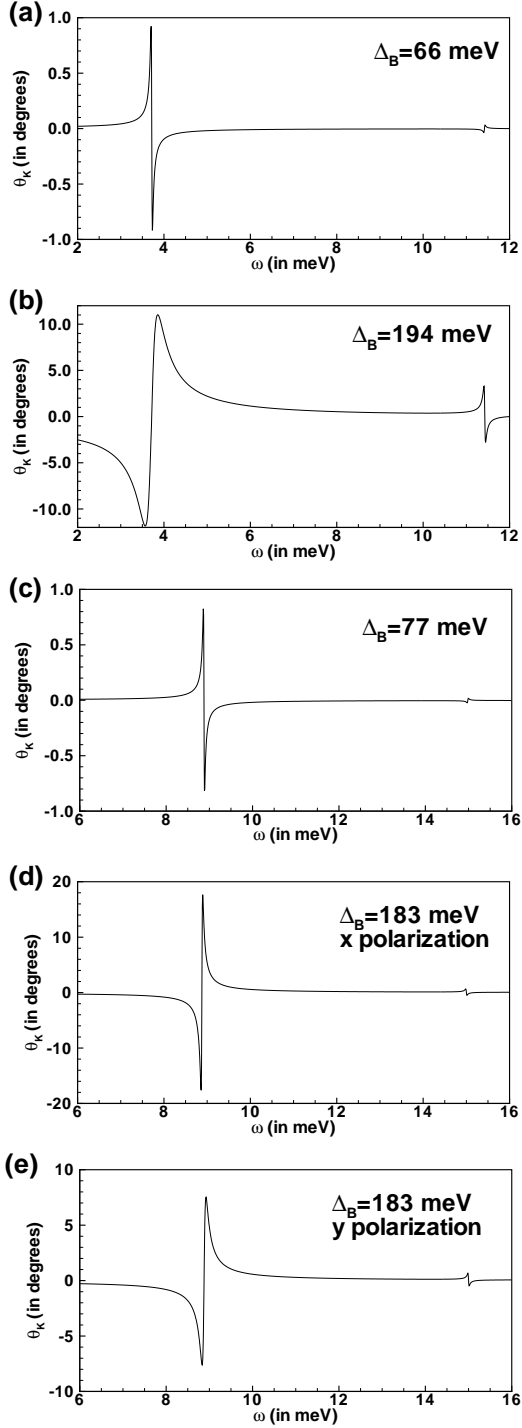


FIG. 13: Kerr angle for conjugate biases (a) $\Delta_B = 66$ meV and (b) $\Delta_B = 194$ meV in the crystal phase and conjugate biases (c) 77 meV and (d) 183 meV in the spiral phase with a x polarization and (e) with a y polarization of the incident wave.

(electromagnetic absorption and Kerr rotation) in the different phases represented in Fig. 1. The absorption frequency can be tuned all the way to zero in the incoherent phase while it is almost constant in the crystal and spiral phase and zero in the uniform state with orbital coherence. The absorption frequency can be modified by applying an electric field in the plane of the layers, but in a limited way since such a field suppresses the nonuniform states. Another clear signature occurs in what we call the conjugate states where the same optically active modes at two conjugate biases are active in opposite circular polarizations. Moreover, the optically active modes in the incoherent and crystal phases are circularly polarized in contrast to the active modes in the spiral phase which are neither completely linearly polarized nor completely circularly polarized.

Another qualitative difference that we find is in the behavior of the Kerr rotation. There is a Kerr effect near the frequency of each mode active in the absorption. Conjugate states show a Kerr effect at the same frequency but with opposite sign for the rotation of the polarization. The maximal polarization angle (near the resonant frequency) is bigger for bias Δ_B above the middle of the spiral phase. The observability of the Kerr effect would depend very much on the strength of the disorder in the sample. A proper treatment of disorder is also necessary to derive the actual absorption line shape due to the collective excitations.

The sequence of phase transitions that we studied in this paper has not been observed so far. We think that the work presented here may help in distinguishing the different phases. Of course, several improvements would be necessary to get numerically accurate predictions. Landau level mixing, for example, is known to modify the dispersion and hence the absorption frequency of the collective modes or magnetoexcitons²⁰. Also, an important information as regards the experimental observability of the phases would be to know how fragile they are with respect to thermal fluctuations. We leave these problems for further work.

Acknowledgments

R. Côté was supported by a grant from the Natural Sciences and Engineering Research Council of Canada (NSERC). Computer time was provided by Calcul Québec and Compute Canada.

¹ For a review of some of the properties of graphene and bilayer graphene, see for example: A. H. Castro Neto,

F. Guinea, N. M. R. Peres, K. S. Novoselov and A.

- K. Geim, *Rev. Mod. Phys.* **81**, 109 (2009); D. S. L. Abergel, V. Apalkov, J. Berashevich, K. Ziegler and Tapash Chakraborty, *Advances in Physics* **59**, 261 (2010); M. O. Goerbig, *Rev. Mod. Phys.* **83**, 1193 (2011); Edward McCann and Mikito Koshino, *Rep. Prog. Phys.* **76**, 056503 (2013).
- ² For a review of the C2DEG in bilayer graphene in Landau level $N = 0$, see for example: Yafis Barlas, Kun Yang, and A. H. MacDonald, *Nanotechnology* **23**, 052001 (2012).
- ³ J. Lambert and R. Côté, *Phys. Rev. B* **87**, 115415 (2013).
- ⁴ E. V. Gorbar, V. P. Gusynin, Junji Jia, and V. A. Miransky, *Phys. Rev. B* **84**, 235449 (2011); E. V. Gorbar, V. P. Gusynin, and V. A. Miransky, *JETP Lett.* **91**, 314 (2010); E. V. Gorbar, V. P. Gusynin, and V. A. Miransky, *Phys. Rev. B* **81**, 155451 (2010); C. Töke and V. I. Fal'ko, *Phys. Rev. B* **83**, 115455 (2011); E. V. Gorbar, V. P. Gusynin, V. A. Miransky, and I. A. Shovkovy, *Phys. Rev. B* **85**, 235460 (2012).
- ⁵ Wenchen Luo, R. Côté, and Alexandre Bédard-Vallée, *Phys. Rev. B* **90**, 075425 (2014).
- ⁶ Yafis Barlas, R. Côté, K. Nomura, and A. H. MacDonald, *Phys. Rev. Lett.* **101**, 097601 (2008).
- ⁷ Benjamin E. Feldman, Jens Martin, and Amir Yacoby, *Nat. Phys.* **6**, 889 (2009); Y. Zhao, P. Cadden-Zimansky, Z. Jiang, and P. Kim, *Phys. Rev. Lett.* **104**, 066801 (2010); R. T. Weitz, M. T. Allen, B. E. Feldman, J. Martin, and A. Yacoby, *Science* **330**, 812 (2010); J. Martin, B. E. Feldman, R. T. Weitz, M. T. Allen, and A. Yacoby, *Phys. Rev. Lett.* **105**, 256806 (2010). Seyoung Kim, Kayoung Lee, and E. Tutuc, *Phys. Rev. Lett.* **107**, 016803 (2011); Seyoung Kim, Kayoung Lee, and E. Tutuc, *Phys. Rev. Lett.* **107**, 016803 (2011); J. Velasco Jr, L. Jing, W. Bao, Y. Lee, P. Kratz, V. Aji, M. Bockrath, C. N. Lau, C. Varma, R. Stillwell, D. Smirnov, Fan Zhang, J. Jung, and A. H. Macdonald, *Nat. Nanotechnol.* **7**, 156 (2012); Seyoung Kim, Insun Jo, D. C. Dillen, D. A. Ferrer, B. Fallahazad, Z. Yao, S. K. Banerjee, and E. Tutuc, *Phys. Rev. Lett.* **108**, 116404 (2012); H. J. Elferen, A. Veligura, E. V. Kurganova, U. Zeitler, J. C. Maan, N. Tombros, I. J. Vera-Marun, and B. J. van Wees, *Phys. Rev. B* **85**, 115408 (2012). P. Maher, C. R. Dean, A. F. Young, T. Taniguchi, K. Watanabe, K. L. Shepard, J. Hone and P. Kim, *Nature Phys.* **9**, 154 (2013); Kayoung Lee, Babak Fallahazad, Hongki Min, and Emanuel Tutuc, *IEEE Trans. Electron Devices* **60**, 103 (2013); K. Lee, B. Fallahazad, J. Xue, D. C. Dillen, K. Kim, T. Taniguchi, K. Watanabe, and E. Tutuc, *Science* **345**, 58 (2014).
- ⁸ R. Côté, Jules Lambert, Yafis Barlas, and A. H. MacDonald, *Phys. Rev. B* **82**, 035445 (2010).
- ⁹ R. Côté, J. P. Fouquet, and Wenchen Luo, *Phys. Rev. B* **84**, 235301 (2011).
- ¹⁰ Jung Hoon Han, Jiadong Zang, Zhihua Yang, Jin-Hong Park, and Naoto Nagaosa, *Phys. Rev. B* **82**, 094429 (2010); Jin-Hong Park and Jung Hoon Han, *Phys. Rev. B* **83**, 184406 (2011).
- ¹¹ M. Orlita and M. Potemski, *Semicond. Sci. Technol.* **25**, 063001 (2010).
- ¹² Iris Crassee, Julien Levallois, Andrew L. Walter, Markus Ostler, Aaron Bostwick, Eli Rotenberg, Thomas Seyller, Dirk van der Marel and Alexey B. Kuzmenko, *Nat. Phys.* **7**, 48 (2011).
- ¹³ Rahul Nandkishore and Leonid Levitov, *Phys. Rev. Lett.* **107**, 097402 (2011).
- ¹⁴ E. V. Gorbar, V. P. Gusynin, A. B. Kuzmenko, and S. G. Sharapov, *Phys. Rev. B* **86**, 075414 (2012).
- ¹⁵ K. Shizuya, *Phys. Rev. B* **79**, 165402 (2009).
- ¹⁶ Edward McCann and Vladimir I. Fal'ko, *Phys. Rev. Lett.* **96**, 086805 (2006).
- ¹⁷ We use the most recent values of these parameters in the present work. See Jeil Jung and Allan H. MacDonald, *Phys. Rev. B* **89**, 035405 (2014).
- ¹⁸ R. Côté and Manuel Barrette, *Phys. Rev. B* **88**, 245445 (2013).
- ¹⁹ L. Wendler and V. G. Grigoryan, *Physica B* **245**, **127** (1998).
- ²⁰ Judith Sári and Csaba Töke, *Phys. Rev. B* **87**, 085432 (2013); Csaba Töke and Vladimir I. Fal'ko, *Phys. Rev. B* **83**, 115455 (2011).